50th AIAA Aerospace Sciences Meeting including the New Horizons Forum and Aerospace Exposition
09 - 12 January 2012, Nashville, Tennessee

AIAA 2012-0413

Lateral Jet Interaction on a Finned Projectile in Supersonic Flow

James DeSpirito[1]

U.S. Army Research Laboratory, Aberdeen Proving Ground, Maryland, 21005

The flow interaction effects from a jet issuing into a supersonic crossflow are investigated using computational fluid dynamic simulations of a basic fin-stabilized projectile at moderate positive and negative angles attack. Data was generated for a high-pressure ratio jet located at seven locations along the projectile axis. Crossflow Mach numbers of 1.5, 2.5, and 3.5 were investigated for an angle of attack range of -10° ≤ α ≤ 10°. Flowfield visualizations indicated the size of the jet plume and the size of the resulting low-pressure region behind the jet were reduced as Mach number increased. The jet force amplification factor showed more variation as α became more negative. The effective jet location was found to vary little for α > -5° at Mach 2.5 and 3.5. For α > -5°, there was less variation of force amplification factor a Mach number increased. Flight simulations using reaction jet "squibs" were performed to evaluate the sensitivity of the control maneuver to the differences in jet thrust and jet actuation location. These results showed that significant differences in the projectile maneuver control were obtained if the effective jet thrust acting at the effective jet location were used instead of the *ideal* jet thrust acting at the jet exit location.

Nomenclature

ANF	=	Army-Navy Finner projectile
AR	=	jet exit-to-throat area ratio
d	=	projectile diameter, m
F_j	=	jet thrust force, N
F_{ji}	=	jet interaction force, N
$F_{j_{eff}}$	=	effective jet force including jet interaction force, N
F_{total}	=	total normal force (thrust + interaction + force due to α), N
$F_{no\text{-}jet}$	=	normal force due to α without jet, N
J	=	jet exit-to-freestream dynamic pressure ratio, q_j / q_∞
K_f	=	jet force amplification factor
K_m	=	jet moment amplification factor
M	=	Mach number
M_j	=	moment induced by jet thrust force, N-m
M_{ji}	=	moment induced by jet interaction force, N-m
$M_{j_{eff}}$	=	effective moment induced by effective jet thrust, N-m
M_{total}	=	moment induced by total normal force, N-m
p_∞	=	freestream static pressure, Pa
p_0	=	freestream total pressure, Pa
p_{0_j}	=	jet total pressure, Pa
PR	=	jet total-to-freestream static pressure ratio, p_{0_j} / p_∞
PR_0	=	jet total-to-freestream total pressure ratio, p_{0_j} / p_{0_∞}
QE	=	launch quadrant elevation, deg.
q_∞	=	freestream dynamic pressure, Pa
q_j	=	jet exit dynamic pressure, Pa
t	=	time, s

---

[1] Aerospace Engineer, WMRD Flight Sciences Branch, RDRL-WML-E, AIAA Associate Fellow.

x_{cp_i}	=	center of pressure due to total, jet, interaction forces, etc., cal.
α	=	angle of attack, deg.
α_T	=	total angle of attack, $\alpha_T = \sqrt{\alpha^2 + \beta^2}$, deg
β	=	angle of side sweep, deg.

I. Introduction

THE study of jets issuing into a cross flow has been the subject of research for about seventy years.[1–3] The primary purpose of such a reaction jet control (RJC) system is to generate a lateral force or moment to provide attitude or roll control of a flight vehicle. There are several advantages of RJC systems over conventional aerodynamic controls such as canards or fins, e.g., increased maneuver authority when operating in low dynamic pressure (low velocity or high altitude), small time delay for actuation effect, and compact design. In addition, the external aerodynamics of the flight vehicle are unaffected except during the actuation period of the jet. The primary disadvantage of a RJC system is the effect of the jet interaction (JI) flowfield on the control forces and moments. Research shows the operation of a lateral reaction jet in atmospheric flight results in an interference flow between the jet plume and the flow over the vehicle.[2,3]

The currently accepted flow structure in the near field of a supersonic jet issuing into a supersonic freestream is illustrated in Fig. 1, as presented by Champigny and Lacau[3] for a flow over a flat plate. One of the main features is due to the jet stream acting as an obstruction to the flow. A shock-boundary layer interaction forms upstream of the jet as the approaching boundary layer interacts with the bow shock, leading to a λ-shock structure. The separated flow in this region wraps around the jet and forms the counter-rotating horseshoe vortices that stay near the wall surface. The jet plume is curved in the direction of the flow due to the freestream flow. A "barrel" shock surrounds the jet plume and terminates in a Mach disk. Two counter-rotating wake vortices form and travel downstream as the primary flow feature of the jet plume. These vortices likely originate from the ring vortices of the jet shear layer as they exit the orifice, which get transformed as they interact with the cross flow.[3]

Figure 1. Accepted flow structure of jet injecting into a supersonic crossflow from a flat plate.[3]

The flow structure in the near field of a supersonic jet issuing from a body of revolution, i.e., a projectile or missile, is similar to that for the flat plate and is shown in Fig. 2 (from Ref. 4). Some differences are that now the jet is located behind the bow shock formed at the nose of the projectile. Also, the jet bow shock and horseshoe vortices emanating from the separation region will tend to "wrap-around" the projectile body. The basic features of the separation region and λ-shock are very similar to that observed with a jet issuing from a flat plate. A strong turbulent wake extends behind the jet and a recompression shock forms downstream.

Figure 2. Schematic of a jet interaction flowfield around a body of revolution.[4]

Accurate prediction of the JI effects is important for predicting the overall forces and moments imparted to the projectile, as the presence of the lateral jet will affect the entire flowfield. The flow disturbances due to the JI will alter the forces and moments that would otherwise be expected to be produced from the jet thrust alone. Since a high-pressure region is produced ahead of the jet and a low pressure region produced behind the jet, a net moment is also produced (nose down for the configuration shown in Fig. 2). The part of the jet bow shock that wraps around the projectile body increases the pressure underneath the projectile, adding to that induced moment. The overall
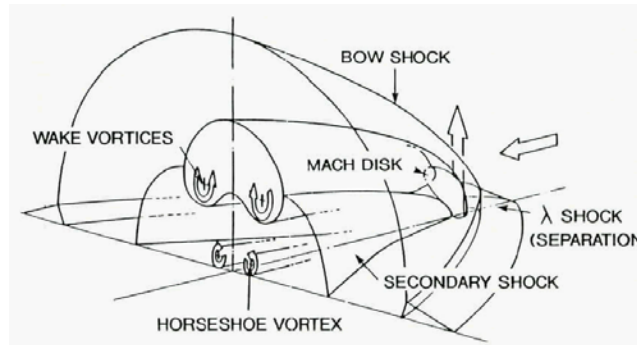
effect is that both the control force and moment produced by the lateral jet may be augmented or attenuated due to JI effects.

Previous studies[5,6] by the author investigated several jet parameters in a supersonic crossflow on both a flat plate validation case and the same finned projectile that is the subject of this paper. The parameters investigated using the flat plate configuration[5] were jet total-to-freestream static pressure ratio (PR), jet exit-to-throat area ratio (AR), freestream Mach number, jet total temperature, and freestream altitude. Some conclusions from the flat plat investigation were[5]

- The JI, as determined from the jet amplification factor, K_f, was most dependent on PR and the freestream Mach number.
- K_f was found to increase with Mach number and decrease with increasing PR.
- There was only a small variation of K_f with AR and the jet gas total temperature.
- There was a strong decrease in K_f with increasing altitude, which was primarily due to the increase in PR as the freestream static pressure decreases with altitude and the jet total pressure was held constant.
- The data show that the jet force is usually amplified ($K_f > 1$) for jets issuing from a flat plate into a supersonic freestream. However, K_f does decrease as the Mach number is reduced, eventually leading to attenuation of the jet force.

The investigation of the jet on the projectile considered the effects of supersonic Mach number, PR, and axial location of the jet along the projectile body. All simulations were performed at zero angle of attack and some conclusions were[5,6]

- Locating the jet near the tail fins minimized the traditional JI effects due to interactions in the jet wake; however, the interaction of the near-jet flowfield with the fins must be taken into account. There is generally an amplification of the jet force when the jet is located very near the tail fins.
- The jet thrust force was attenuated about 15-45% at Mach 2.5 and about 25-75% at Mach 1.5 for the forward five jet locations. The jet thrust force was amplified by 70-80% at Mach 2.5 and 6-80% at Mach 1.5 for the two rear locations.
- In all cases, the effective jet location $x_{cP_{eff}}$, was either forward of the jet location or very close to it, e.g., when the jet was located near the tail.
- Comparisons of the results with those from a body alone (no tail fins) configuration showed that the jet flow interactions with the tail are minimal when the jet is located toward the nose of the projectile.

The features of the jet interaction flowfield for both the flat plate and the projectile compared well with those presented and described in the archival literature. The choice of turbulence model was also found to affect accurate prediction of the features of the interaction flowfield. In the flat plate configuration, differences of up to 13% and 15% were observed in the force amplification factor and JI force, respectively, among the results for seven turbulence models.
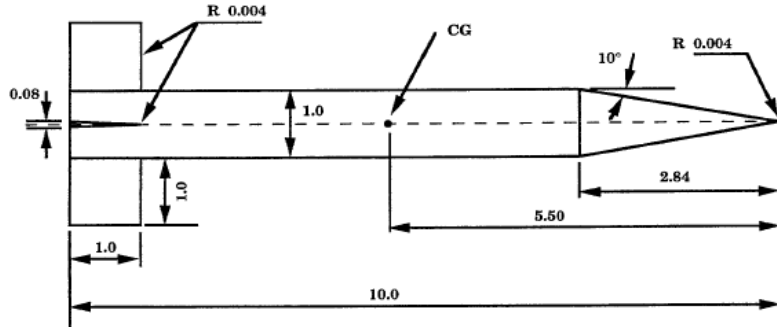
The goal of this work is to generate an extensive JI database on one projectile configuration in the hope of determining correlations for effective jet force and effective jet location that may be used in aeroprediction design codes. It is understood that this is likely a challenging task, as the JI effects can be very configuration dependent. While the JI effects of many of these parameters have been reported in the literature, the range of data available for each configuration (e.g., M, α, jet characteristics, etc.) is usually limited. Generating data for all the parameters on one flight vehicle configuration reduces the number of variables in the database.

The first part of this study was conducted at zero angle of attack.[5,6] The present work extends that work by investigating the effects of moderate positive and negative angles of attack on the JI and including a third supersonic Mach number of 3.5. A high pressure ratio air jet issuing into a supersonic crossflow was investigated for projectile angles of attack of $-10° \leq \alpha \leq 10°$, and Mach number of 1.5, 2.5, and 3.5. A sonic jet nozzle (exit-to-throat area of unity) was positioned at seven locations along the projectile axis. In addition, six degree-or-freedom (6DOF) trajectory simulations were performed to quantify the effects of the ideal jet thrust (unattenuated, acting at nozzle exit location) vs. effective jet thrust (attenuated, acting at effective jet location) on both an extended range and a side deflection maneuver.

American Institute of Aeronautics and Astronautics

II. Approach

A. Army-Navy Finner Model

The basic Army-Navy Finner (ANF) projectile[7,8] was used as the flight vehicle in this study, as a large database of archival experimental data exists for this configuration. The geometry of the ANF is shown in Fig. 3. It is a basic cone-cylinder design, 10 cal. long with a 2.84 cal. (1 cal. = 30 mm) conical nose. There are four uncanted, 1-cal. square planform fins mounted flush with the base of the projectile. The c.g. is located 5.5 calibers from the nose of the

Figure 3. Army-Navy (Basic) Finner Missile Geometry (dimensions in cal., d = 30 mm).[8]

projectile. Seven jet locations were investigated; all located on the upper surface. The jet locations are listed in Table 1, along with a description of where they are relative to projectile features.

Table 1. Jet Locations Along Army-Navy Finner Projectile.

| Label	Location from nose		Location from c.g.		Description
	(mm)	(cal.)	(mm)	(cal.)	
F3	65.0	2.17	-100.0	-3.33	On conical nose
F2	90.0	3.00	-75.0	-2.50	Just rearward of cone
F1	127.5	4.25	-37.5	-1.25	Between cone and c.g.
F0	165.0	5.50	0.0	0.00	At c.g.
R1	215.0	7.17	50.0	1.67	Between c.g. and tail fins
R2	265.0	8.83	100.0	3.33	Just ahead of tail fins
R3	290.0	9.67	125.0	4.17	Between tail fins

B. Computational Details

The forward edge of the domain starts 5 cal. in front of the projectile; the end of the domain is 20 cal. behind the projectile base; and the radial extent of the domain is 14.5 cal. from the projectile body surface. The computational domain was meshed with MIME from Metacomp Technologies.[9] The mesh consisted of tetrahedral cells and triangular prism layers projected from the solid wall surfaces. Using the symmetry of the system, only a half model was meshed. Some simulations were performed with a full computational domain, without the assumption of symmetry, to determine if there were any asymmetric JI effects. Several jet exit locations (F3, F1, F0, R3), Mach numbers (1.5, 2.5), and α (0°, -5°, -10°) were investigated. No lateral (side) force or (side, roll) moments were found induced by the JI; indicating that the half-domain simulations were adequate for predicting the JI effects induced in this configuration at the flow conditions under consideration. One mesh was used to run all cases; a smaller domain for the higher Mach number cases did not result in significant mesh size savings due to the density boxes located close to the projectile.

The meshes on the symmetry plane and projectile surfaces are shown in Fig 4. Density boxes, which allow finer control of the mesh characteristics, are used to refine the mesh in expected regions of high gradients. Figures 4a-c show the density boxes used around the whole projectile, the wake, and in the JI region. Two density boxes used for the JI region were moved along the projectile as the jet location moved. Figure 4b shows the mesh for the jet in the F0 location, while Figure 4c shows the mesh for the jet in the F2 location. As the jet location was moved rearward there was a small reduction in the required mesh size. The total mesh sizes ranged from 8.8 M cells for the jet in the R3 location to 10.2 M cells for the jet in the F3 location. The mesh in the nozzle exit region (Fig. 4f) was continuous, i.e., no boundary surface was at the exit. The boundary layer mesh conformed to the nozzle and projectile wall interface and a separate density box was used in the exit region.

All solid surfaces were modeled as no-slip, adiabatic walls. A symmetry boundary condition was used on the symmetry plane. The outer boundaries were modeled using a characteristics based inflow/outflow condition, which is based on solving a Riemann problem at the boundary. The inlet to the nozzle plenum (Fig. 4d) was modeled as a subsonic reservoir boundary inflow with a specified total temperature and pressure. This is a preferred method of directly modeling the nozzle geometry, rather than imposing a boundary condition at the jet exit. There is only a relatively small cost in increased mesh size.

(a)

(b)

(c)

(d)

(e)

(f)
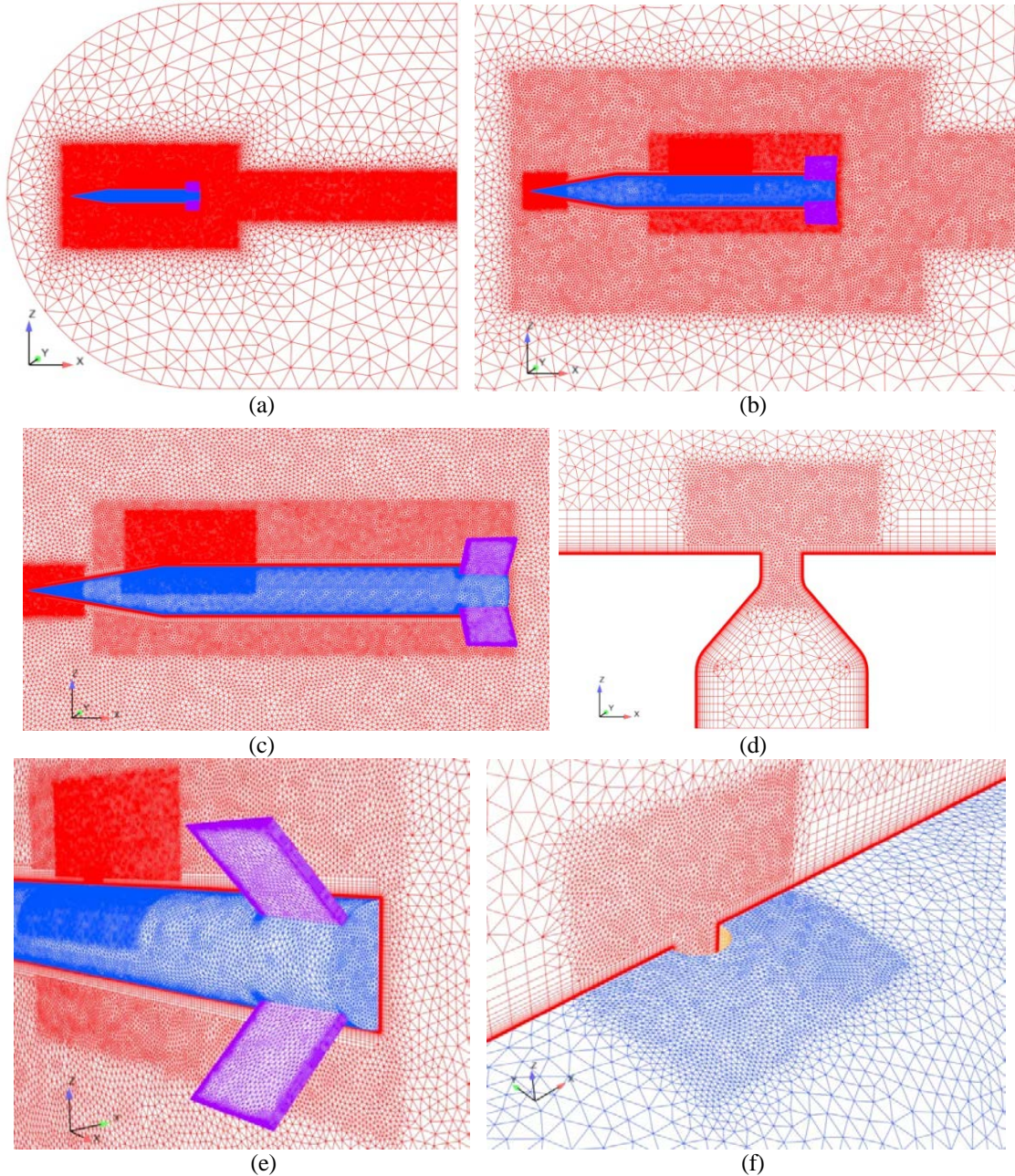
Figure 4. Geometry and mesh used for ANF simulations: (a) symmetry plane of computational domain, (b) density boxes for F0 jet location, (c) density boxes for F2 jet location, (d) sonic nozzle, (e) surface meshes on projectile and symmetry plane, and (f) surface mesh near nozzle exit.

Prism layers were used along all solid boundaries, including the nozzle plenum and throat. The projectile and fin surfaces were modeled with the "solve-to-wall" methodology. The first cell wall spacing was 0.001 mm, resulting

in y^+ values less than 1.0 everywhere except in the interaction region directly in front of the jet, where the values were still less than 2.0. The y^+ values were found to be between 50 and 100 on the nozzle exit walls, due to the different flow properties from the gas expansion there. Therefore, the plenum and nozzle exit walls were modeled with an advanced two-layer wall function boundary condition that reverts to a solve-to-wall method where the mesh is fine enough; or else to a wall function, as on the nozzle walls.

The freestream conditions were based on standard sea level conditions: a static pressure of 101325 Pa and a static temperature of 288 K for Mach 1.5 (510.4 m/s), Mach 2.5 (850.7 m/s), and Mach 3.5 (1191.0 m/s) flows. The jet total temperature was 2700 K and the jet total pressure was 34.5 MPa. Table 2 lists freestream total and dynamic pressure at the three Mach numbers investigated. Also listed are the jet-to-freestream pressure ratio defined in three ways: jet total-to-freestream static, jet total-to-freestream total, and jet dynamic-to-freestream dynamic pressure ratio. As Mach number increases, PR_0 and J decrease as $p_{0\infty}$ and q_∞, respectively, increase while p_{0_j} remains constant. PR is constant since sea level flight conditions (constant p_∞) are assumed.

Table 2. Comparison of pressure ratios ($F_j = 34.5$ MPa, $q_j = 1.28 \times 10^7$ Pa)

M	$p_{0\infty}$ (Pa)	q_∞ (Pa)	PR	PR_0	J
1.5	3.72×10^5	1.60×10^5	340.5	92.8	80.0
2.5	1.73×10^6	4.43×10^5	340.5	19.9	28.8
3.5	7.73×10^6	8.69×10^5	340.5	4.46	14.7

The commercially available CFD++ code,[10] version 11.1, was used in this study. The 3-D, compressible, Reynolds-averaged Navier-Stokes (RANS) equations are solved using a finite volume method. A point-implicit time integration scheme with local time-stepping, defined by the CFL (Courant-Friedrichs-Lewy) number, was used to advance the solution towards steady-state. The multigrid W-cycle method with a maximum of 4 cycles and a maximum of 20 grid levels was used to accelerate convergence. Implicit temporal smoothing was applied for increased stability, which is especially useful where strong transients arise. The inviscid flux function was a second-order, upwind scheme using a Harten-Lax-van Leer-Contact (HLLC) Riemann solver and a multi-dimensional Total-Variation-Diminishing (TVD) continuous flux limiter.[10]

The choice of turbulence model is a key factor in the numerical modeling of complex flows such this, and CFD++ has available a large set of turbulence models. For this study, the two-equation Menter's Shear Stress Transport (SST) model[11] was used. However, no single turbulence model has shown to be able to accurately predict all aspects of the jet interaction (discussed further in Sect. III.A).[5]

The CFL number was typically ramped from 0.1 to about 20 over the first 200 iterations. Divergence checks within CFD++ reduced the final CFL number during the first 1000 to 1500 iterations to between 5 and 10, depending on configuration and freestream Mach number. Some cases were restarted at 2400 iterations with a successful ramping of the CFL number to 30 or 40. Other cases were let run to 3600 iterations with a final CFL of about 10. Although CFL numbers up to 40 are typically used for the freestream Mach numbers used in this study, the Mach number in the jet plume is much higher and the CFL numbers used are more typical of hypersonic flow and lead to more stable convergence. Convergence was determined by a 5-6 order decrease in the magnitude of the maximum residuals and ensuring that the integrated forces and moments on the projectile were not changing with increased iterations. The mass and energy flux through the jet orifice was also tracked and usually converged before the projectile forces and moments. Typically, 3600 to 4800 iterations were required to converge to steady state solutions. The calculations took an average of about 7-10 s of CPU time per iteration when the mesh was partitioned on 64 cores, with approximately 150,000 cells per CPU core. Simulations were performed on a SGI Altix ICE 8200 (HAROLD) Supercomputer at the Army Research Laboratory DoD Supercomputing Resource Center (DSRC) at Aberdeen Proving Ground, MD and a Cray XE6 (RAPTOR) at the Air Force Research Laboratory DSRC at Wright-Patterson Air Force Base, OH.

C. Jet Amplification Factors and Effective Jet Location

The jet amplification factor is a measure of the effect that the JI has on the control forces and moments. The jet force and moment amplification factors are defined as

$$K_f = \frac{F_j + F_{ji}}{F_j}, \tag{1}$$

and

$$K_m = \frac{M_j + M_{ji}}{M_j}.$$
(2)

An amplification factor greater than one indicates the JI effect increases the effectiveness of the jet thrust force, F_j, or the moment induced by the jet thrust, M_j. If the body, such as a projectile, is at an angle of attack, the force or moment induced by the angle of attack—with the jet off—is subtracted from that resulting with the jet on, e.g.,

$$F_{ji} = F_{\text{total}} - F_{\text{no-jet}} - F_j,$$
(3)

where F_{total} is total force due to the jet thrust, JI effects, and angle of attack. $F_{\text{no-jet}}$ is the force in the absence of the jet, which will be non-zero at non-zero α. Moments due to these forces follow directly and the equations using coefficients are similar. On a flat plate or a projectile at zero angle of attack, the JI force and moment are computed directly, since there is no force normal to the surface with the jet off. All moments are referenced from the c.g., so the center of pressure locations are calculated from

$$x_{\text{cp}_{\text{total}}} = \frac{-M_{\text{total}}}{F_{\text{total}}}, \qquad x_{\text{cp}_j} = \frac{-M_j}{F_j}, \qquad x_{\text{cp}_{ji}} = \frac{-M_{ji}}{F_{ji}}, \qquad x_{\text{cp}_{\text{eff}}} = -\frac{M_j + M_{ji}}{F_j + F_{ji}} = -\frac{M_{j_{\text{eff}}}}{F_{j_{\text{eff}}}},$$
(4)

for the *total*, *jet thrust*, *interaction*, and *effective* forces or moments, respectively. A positive x_{cp} indicates a location to the rear of the c.g., while a negative x_{cp} indicates a location forward of the c.g. A nose-down or nose-up rotation about the c.g. depends on the sign of the moment, with a negative moment indicating a nose-down rotation. In the previous work,[5] $x_{\text{cp}_{\text{total}}}$ was used as the effective location that the jet acted, or the resultant force center of pressure (RFCP). This is correct since that total force with no jet, $F_{\text{no-jet}}$, is zero at zero angle of attack. However, at non-zero angle of attack, the RFCP location should properly be calculated as $x_{\text{cp}_{\text{eff}}}$ in Eq. (4), where only the jet and JI forces and moments are considered; and the force due to the projectile angle of attack, $F_{\text{no-jet}}$, is removed.

III. Results and Discussion

A. Turbulence Model Investigation

   The results of a turbulence model investigation using a flat plate validation case was reported previously.[5] Those results were somewhat inconclusive, with different models performing better in different parts of the flow and different crossflow Mach numbers. An estimate of the potential error from using seven different turbulence models was made by comparing the standard deviation of K_f (8–13%) and F_{ji} (10–16%).

   A similar study was conducted using the ANF projectile at $\alpha = 0°$ with the jet exit at the F2 location in a Mach 1.5 crossflow. The same seven turbulence models were used in the present investigation: (i) Menter's Shear Stress Transport (SST) 2-equation model[11] (ii) Spalart-Allmaras's (SA) 1-equation model,[12] (iii) the Realizable k-ε (RKE) 2-equation model,[13] (iv) the cubic k-ε (CKE) non-linear, 2-equation model,[14] (v) Goldberg's R_t (RT) 1-equation model,[14] (vi) Goldberg's k-ε-R (KER) 3-equation model,[15] and the (vii) Reynolds Stress Transport (RSM) 2nd moment closure, 7-equation model.[16] Table 3 presents the summary of the results in the form of percent standard deviation among the results for the seven turbulence models. The percent standard deviation of the jet force and moment amplification factors and the JI force are reasonable—about 5% or less. The largest potential error (36%) is in the prediction of the JI moment, and the resulting center of pressure, $x_{\text{cp}_{ji}}$, which is likely due to differences in the prediction of the surface pressures for difference turbulence models, similar to that observed in the flat plate.[5] However, note that the potential error in the effective jet location, $x_{\text{cp}_{\text{eff}}}$, is only about 4%, as it includes the jet force at a known location and the effect of differences in the predicted JI on this value are reduced. As stated in Sect. II.B, the SST model was used for the remaining simulations.

Table 3. Results from turbulence model study (F2 jet location, $M = 1.5$, $\alpha = 0°$, $F_j = 215.6$ N).

Model	K_f	F_{ji} (N)	K_m	M_{ji} (N-m)	$x_{cp_{ji}}$ (cal.)	$x_{cp_{eff}}$ (cal.)
SST	0.74	55.2	1.06	-0.94	0.57	-3.55
SA	0.76	51.4	1.06	-0.95	0.62	-3.48
RT	0.75	52.7	1.12	-1.89	1.19	-3.70
RKE	0.75	53.2	1.16	-2.54	1.59	-3.84
CKE	0.76	52.9	1.15	-2.39	1.51	-3.80
KER	0.76	52.4	1.15	-2.41	1.54	-3.80
RSM	0.79	45.8	1.11	-1.80	1.31	-3.53
Average	0.76	51.9	1.11	-1.85	1.19	-3.67
Std. Dev.	0.01	2.94	0.04	0.67	0.43	0.15
% Std. Dev.	1.78	5.66	3.74	-36.5	36.2	-4.05

B. $\alpha = 0°$ Cases at Mach 3.5

The previous investigation[5,6] was performed with a sonic jet nozzle positioned at the seven jet locations listed in Table 1, at Mach 1.5 and 2.5, with the projectile at zero angle of attack to the oncoming flow. Those results confirmed previous findings from the literature that the choice of location for a reaction jet can have a significant effect on the JI effects on the resulting aerodynamic forces and moments. Figures 5 and 6 present the force and moment amplification factor variation with jet location and Mach number for the zero angle of attack case. These figures correspond to Fig. 16 of Ref. 5 with the data for Mach 3.5 now included. The data show a decreasing jet force modulation (K_f closer to 1.0) with increasing Mach number. The one exception is when the jet is directly in front of the fins (R2 location), where the jet force amplification at Mach 3.5 is double that at Mach 1.5. There is less variation of K_f and K_m with Mach number as the jet location moves farther forward of the projectile c.g. At Mach 3.5, K_f is relatively constant from the forward (F3) jet location to the mid-body (R1) jet location. As Mach number decreases, the attenuation of the jet increases as the jet location moves rearward to the R1 location. When the jet is directly in front of the fins (R2 location), the jet is amplified and this amplification increases with Mach number. There is again less variation of K_f and K_m with Mach number when the jet is located between the fins (R3 location). As noted in Ref. 5, in general, K_m was near 1.0 (neutral) or amplified at most locations. The R1 location showed $K_m < 0$ for Mach 1.5 and 2.5 (effective jet moment attenuated but in the direction opposite the moment induced by the jet thrust alone). At Mach 3.5, the effective jet moment is attenuated and $K_m > 0$.
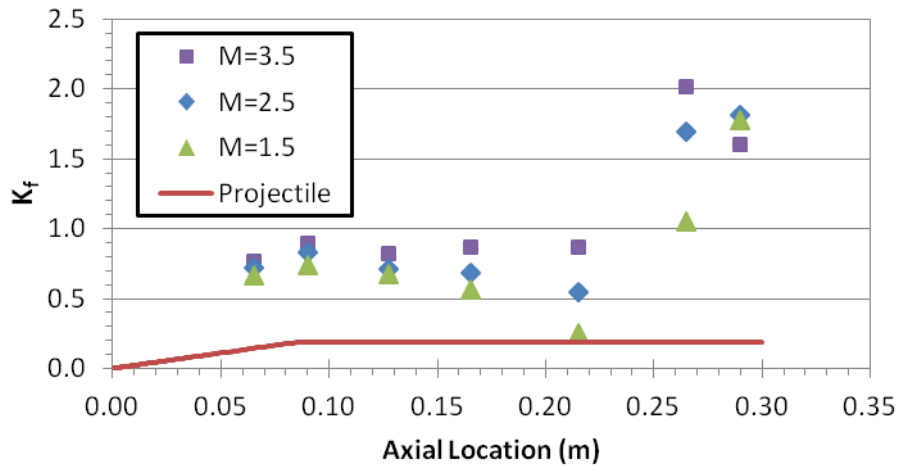

Figure 5. Force amplification factors vs. jet location and Mach number.
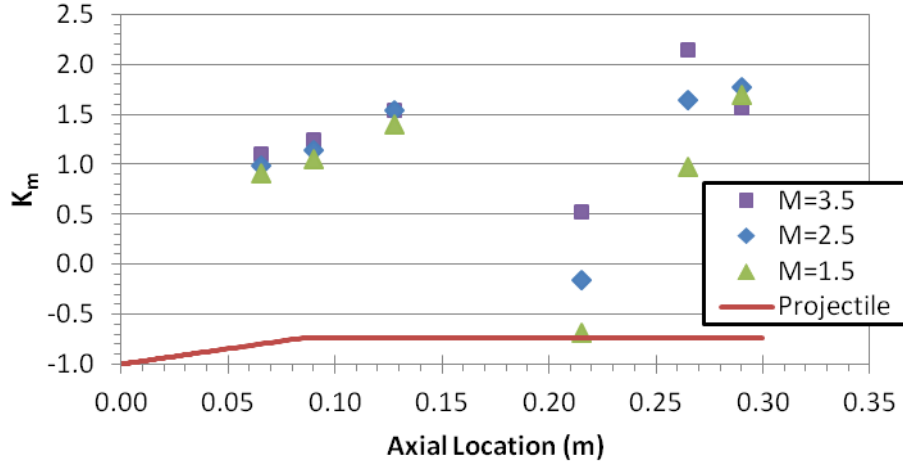
Figure 6. Moment amplification factors vs. jet location and Mach number.

The variation with Mach number is not surprising, as the JI effect is due to the complex interaction of the jet plume and the resulting jet bow shock with the projectile body. Figure 7 shows the variation of the jet interaction flowfield and surface pressure on the projectile with Mach number. As Mach number increases, the size of the jet plume decreases due to the higher freestream dynamic pressure. As shown in Table 2, in these simulations, the jet total-to-freestream pressure ratio stays constant as Mach number increases because sea level flight conditions are used. However, the jet total-to-freestream total pressure and the jet exit-to-freestream dynamic pressure ratios both decrease as Mach number increases because the jet total pressure is constant. This is a realistic case, since the jet thruster will likely be due to a defined energetic charge (constant p_{0_j}) regardless of flight condition.

(a)

(b)

(c)
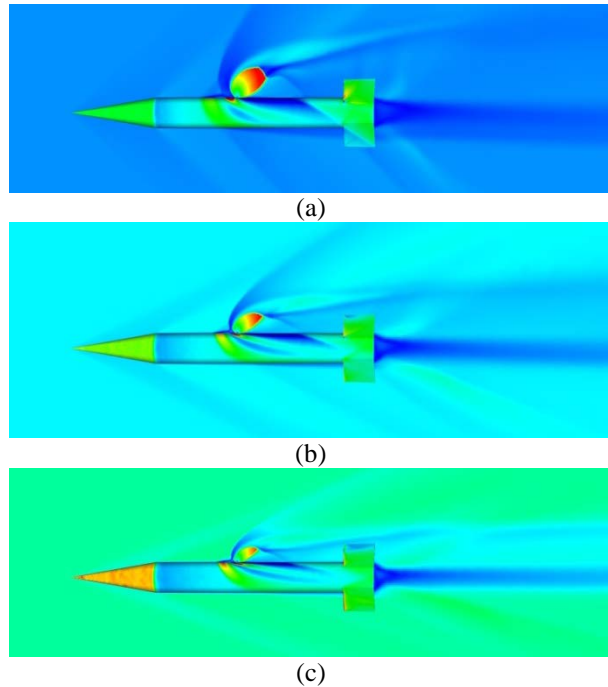
Figure 7. Pressure ratio on projectile surfaces, Mach number on symmetry plane for (a) Mach 1.5, (b) Mach 2.5, and (c) Mach 3.5; F0 jet exit location, $\alpha = 0$. (scales: $0.5 \leq P/P_\infty \leq 2.0$; $0 \leq M \leq 10.0$)

American Institute of Aeronautics and Astronautics

In addition to the decreased size of the jet plume, Fig. 7 shows the different shock interactions and JI induced pressure variations on the projectile surface as the Mach number varies. Generally, as Mach number increases, the size of the high-pressure region ahead of the jet bow shock increases, while the size of the low-pressure region directly behind the jet decreases. The horseshoe vortices emanating from near the jet exit also extend around the projectile body to a lesser extent as Mach number increases, as indicated by the low-pressure streak curving around the body from just ahead of the jet exit.

C. Effect of α on JI

To determine the effect of angle of attack on the jet interaction effects, simulations were performed at $\alpha = \pm 5°$, and $\pm 10°$. Some configurations were also run at $\alpha = \pm 2.5°$. Figure 8–10 show the variation of the flowfield and pressure surface pressure with α for the F0, F3, and R3 jet locations, respectively, at Mach 2.5. In general, the effects of α on the jet interaction flowfield is what might be expected: a negative α tends to force the counter rotating vortex pair (CVP) closer to the projectile surface, while a positive α tends to force the CVP away from the projectile surface, both as compared to the $\alpha = 0°$ case. This effect is most evident for the jet locations forward of the tail, i.e., the F0 and F3 locations. For the R3 location, the CVP is located behind the projectile and will have little or no effect on the projectile surface pressures. Figures 8 and 9 also show significant differences of the pressure distributions along the projectile as α changes. Figure 10 gives an indication of the effect of α only on the forebody pressure distributions; as the jet will have no effect on the forward sections in supersonic flow.

Figures 11 and 12 show the variation of the flowfield and surface pressure with α at Mach 1.5 and 3.5 for the F0 and F3 jet locations, respectively. Qualitatively similar effects are shown for each Mach number. However, while at $\alpha = 0°$ it was noted (Fig. 7) that the low-pressure region behind the jet decreases as Mach number increases, the opposite occurs when the projectile is at $\alpha = 10°$ (Figs. 8–12).

The effects of angle of attack on the force and moment amplification factors are shown in Figs. 13–15 for Mach 1.5, 2.5 and 3.5, respectively. At Mach 1.5 (Fig. 13) there is generally a decreasing trend of K_f as angle of attack decreases. At the locations forward of the c.g. (F1–F3) K_f is fairly constant for $0° \leq \alpha \leq 10°$. At Mach 2.5 (Fig. 14) K_f is reasonably constant at all locations for $-5° \leq \alpha \leq 10°$. At $\alpha = -10°$ K_f noticeably decreases at the F3 location and increases at the R3 location. At Mach 3.5 (Fig. 15) there is again a decreasing trend of K_f as angle of attack decreases for the locations R1 and forward. K_f decreases with *increasing* angle of attack at the R2 location and has a slight minimum at $\alpha = 0°$ at the R3 location. Corresponding trends can be described for K_m, also shown in Figs. 13–15, but the moment is more sensitive due to the combined effects of the variation of K_f and $x_{cp_{eff}}$.

It is also useful to look at the *effective jet location*, $x_{cp_{eff}}$, which is determined from the jet and JI forces and moment only (i.e., $F_{j_{eff}} = K_f F_j$ and $M_{j_{eff}} = K_m M_j$, see Eqs. 1, 2, and 4). These are shown in Fig. 16a–c for the Mach 1.5, 2.5, and 3.5, respectively. The units of $x_{cp_{eff}}$ are in calibers relative to the projectile c.g. (the projectile spans the range $-5.5 \leq x \leq 4.5$). As noted in Ref. 5, it is observed that the effective jet location remains very near the jet exit location (see Table 1) when the jet is located near the tail (R2 and R3 locations) at $\alpha = 0$. At these two rearward locations, $x_{cp_{eff}}$ is also unaffected by angle of attack at all three Mach numbers.

The effective jet location is forward of the jet exit at all three Mach numbers and $\alpha = 0$ for all jet exit locations except the R2 and R3 locations. This is because the JI produces an upward force behind the jet, which, combined with the downward force in front of the jet (due to the high-pressure compression region behind the jet bow shock), produces an amplified jet-induced moment. Then, the effective jet location must move forward, especially since the jet thrust is attenuated at these locations. At Mach 1.5, $x_{cp_{eff}}$ decreases with decreasing α; and at a higher rate for $\alpha < 0°$. The variation of $x_{cp_{eff}}$ with α at the R1 location is also large at Mach 1.5. These trends are consistent with the variation of K_f with α, as shown in Fig. 13a. Note that $x_{cp_{eff}}$ is actually predicted to be forward of the projectile nose in some cases, especially the forward jet locations at $\alpha < 0$. Remember that this *effective* center of pressure is based only on the jet and JI forces and moments. When the force and moment due to α (without a jet present) are also considered, the center of pressure usually resided on the projectile body. The exception was for a few cases when the *total* force approached zero ($F_{total} \rightarrow 0$), leading to increased values of $x_{cp_{total}}$. At Mach 2.5 and 3.5 (Figs. 16b,c), there is very little variation of $x_{cp_{eff}}$ with α for $-5° \leq \alpha \leq 10°$. This again is consistent with the trends of K_f shown in Figs. 14 and 15. No data is shown in Fig. 16c for the F3 location at $\alpha = -10°$ as $F_{j_{eff}} \rightarrow 0$ for that case and $x_{cp_{eff}}$ became indeterminate.
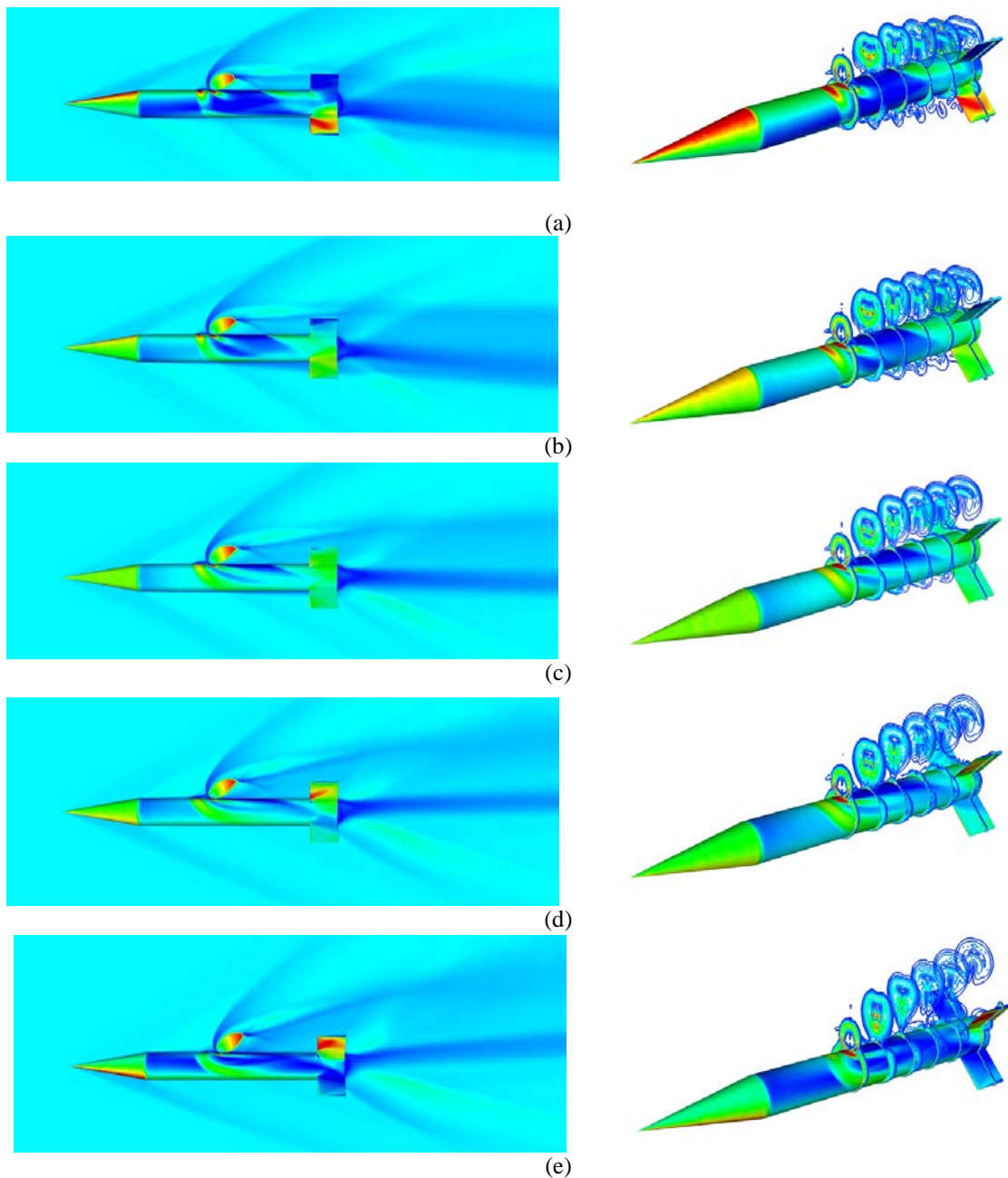
Figure 8. Pressure ratio on projectile surfaces, Mach number on symmetry plane (left) and vorticity contours on axial planes (right) for Mach 2.5, F0 jet exit location, (a) α = -10°, (b) α = -5°, (c) α = 0°, (d) α = 5°, and (e) α = 10°. (scales: $0.5 \leq P/P_\infty \leq 2.0$; $0 \leq M \leq 10.0$)
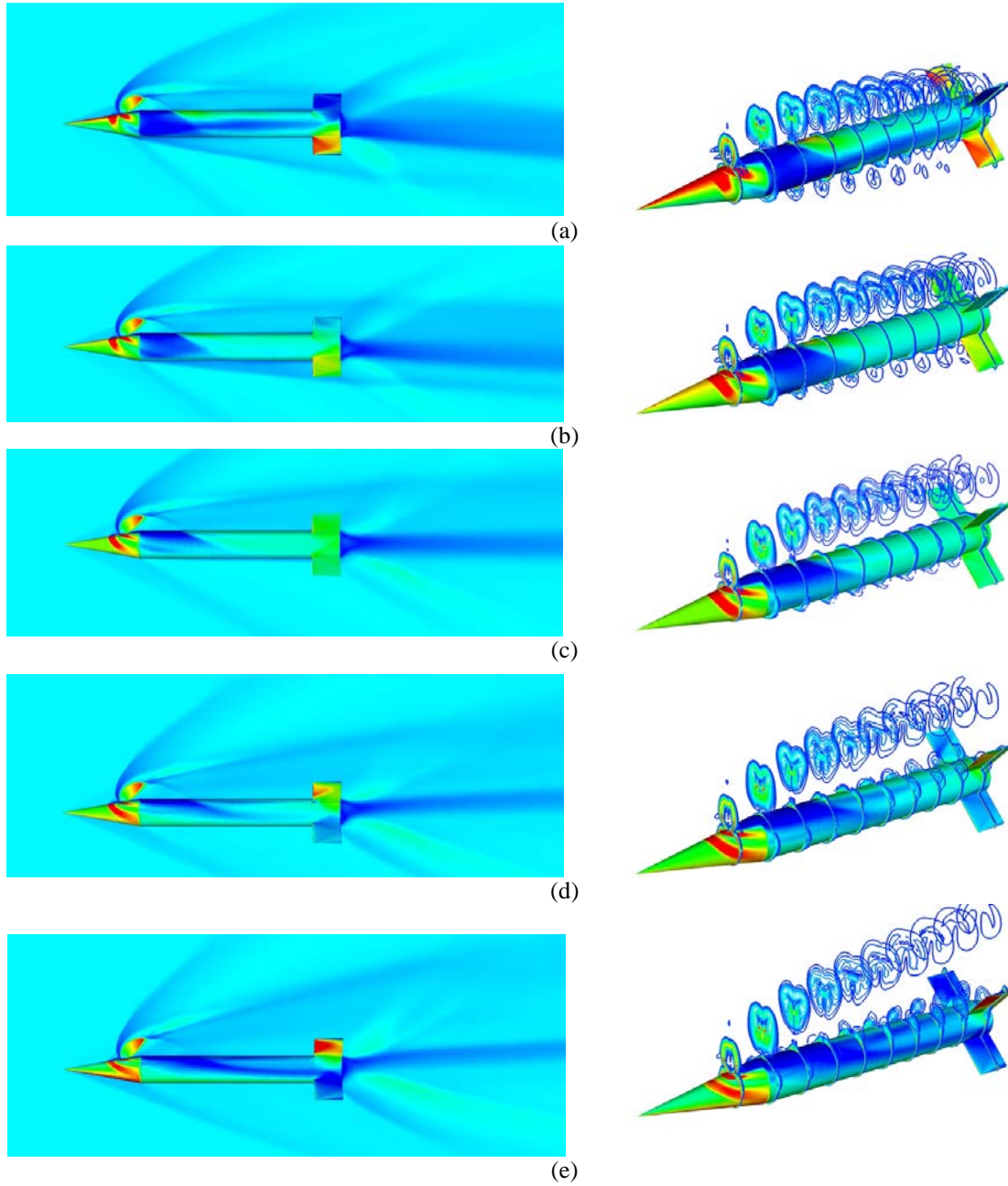
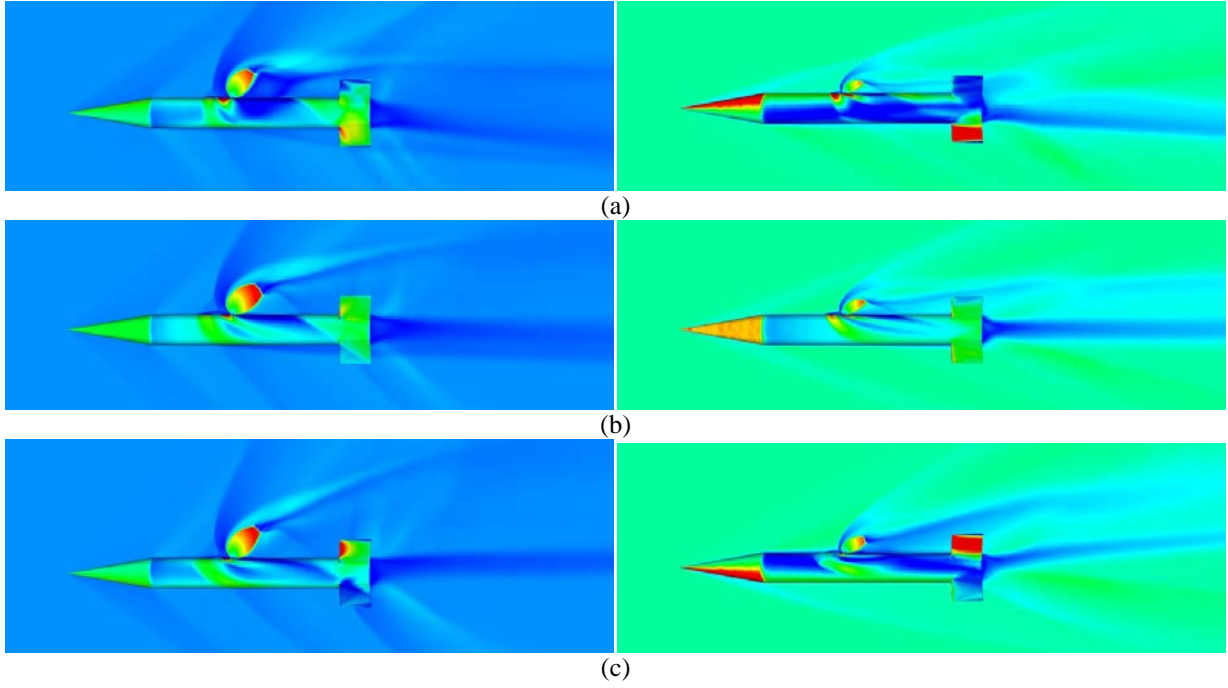**Figure 9. Pressure ratio on projectile surfaces, Mach number on symmetry plane (left) and vorticity contours on axial planes (right) for Mach 2.5, F3 jet exit location, (a) α = -10°, (b) α = -5°, (c) α = 0°, (d) α = 5°, and (e) α = 10°. (scales: $0.5 \leq P/P_{\infty} \leq 2.0$; $0 \leq M \leq 10.0$)**

(a)

(b)

(c)

(d)

(e)
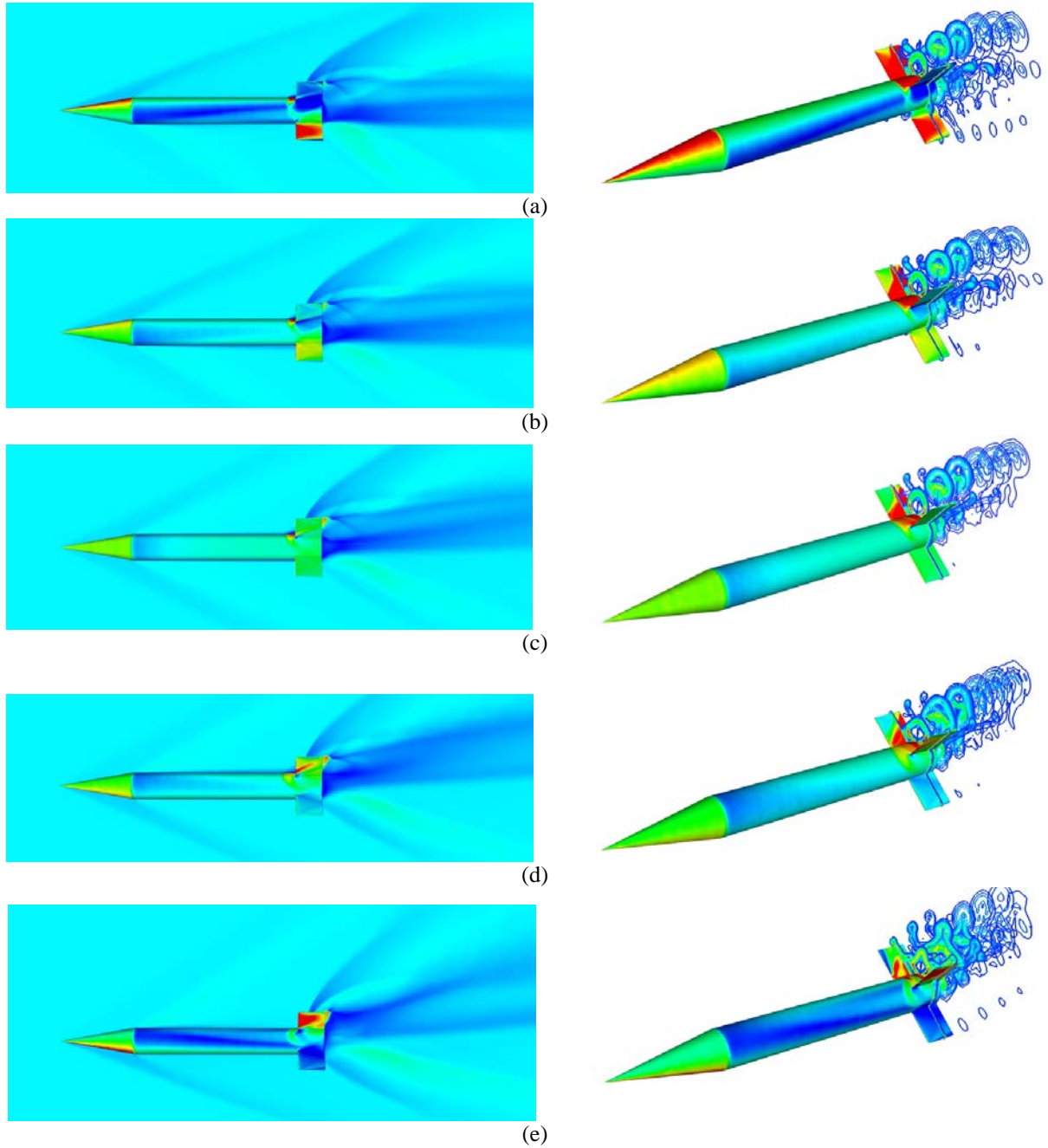
Figure 10. Pressure ratio on projectile surfaces, Mach number on symmetry plane (left) and vorticity contours on axial planes (right) for Mach 2.5, R3 jet exit location, (a) α = -10°, (b) α = -5°, (c) α = 0°, (d) α = 5°, and (e) α = 10°. (scales: $0.5 \leq P/P_\infty \leq 2.0$; $0 \leq M \leq 10.0$)
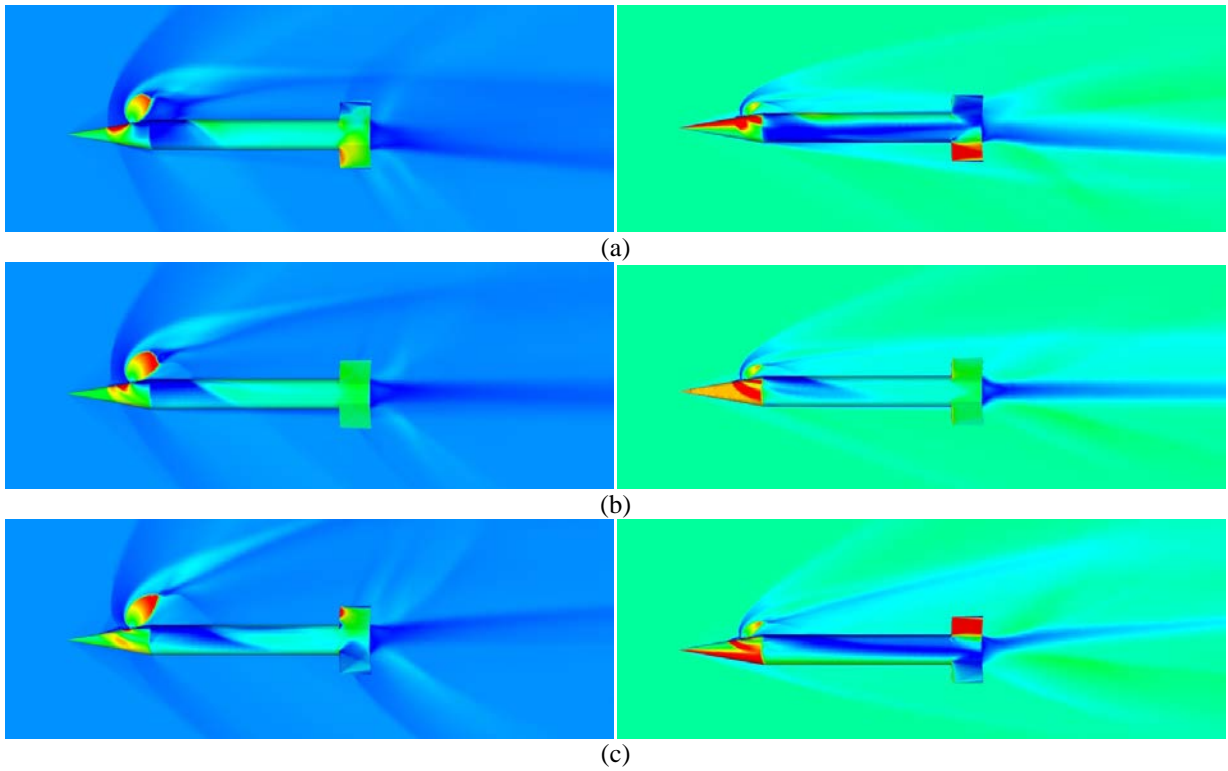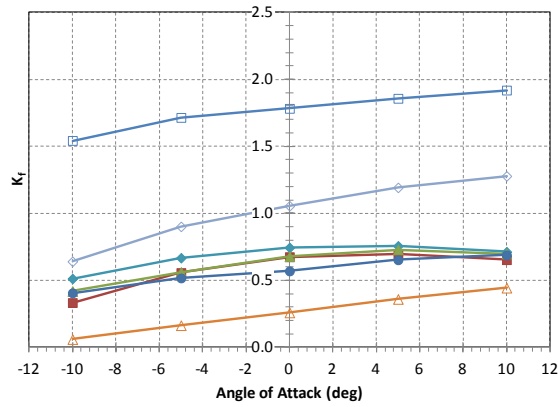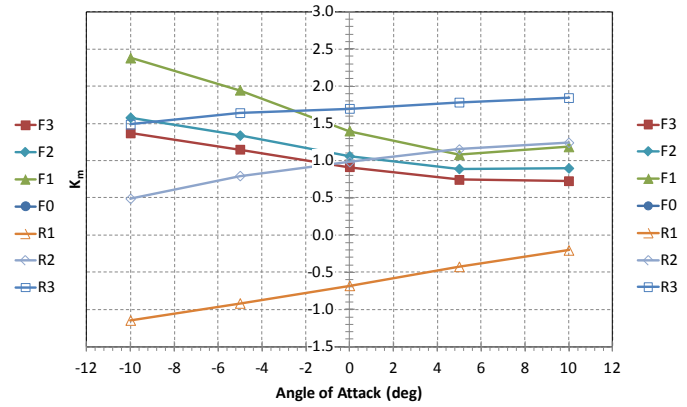
Figure 11. Pressure ratio on projectile surfaces, Mach number on symmetry for Mach 1.5 (left) and Mach 3.5 (right), F0 jet exit location, (a) α = -10°, (b) α = 0°, (c) α = 10°. (scales: $0.5 \leq P/P_\infty \leq 2.0$; $0 \leq M \leq 10.0$)

Figure 12. Pressure ratio on projectile surfaces, Mach number on symmetry for Mach 1.5 (left) and Mach 3.5 (right), F3 jet exit location, (a) α = -10°, (b) α = 0°, (c) α = 10°. (scales: $0.5 \leq P/P_\infty \leq 2.0$; $0 \leq M \leq 10.0$)
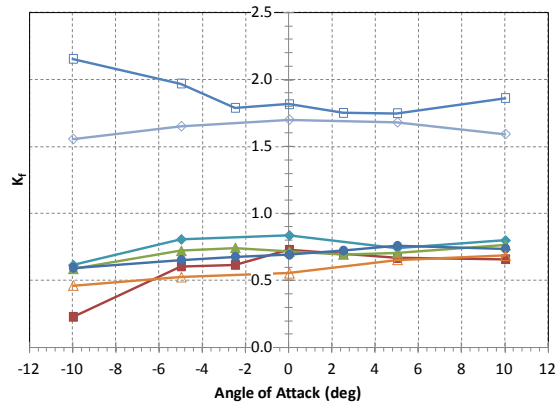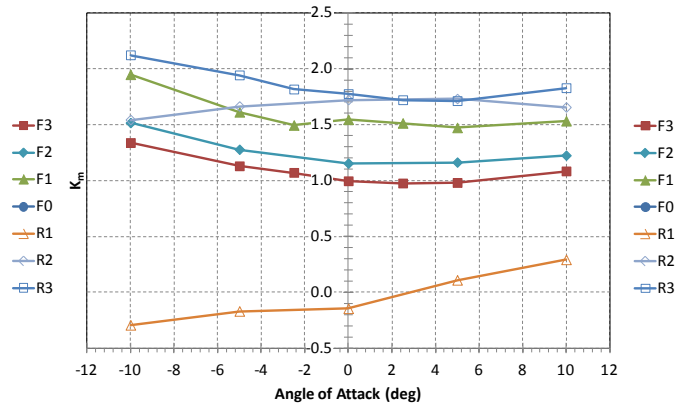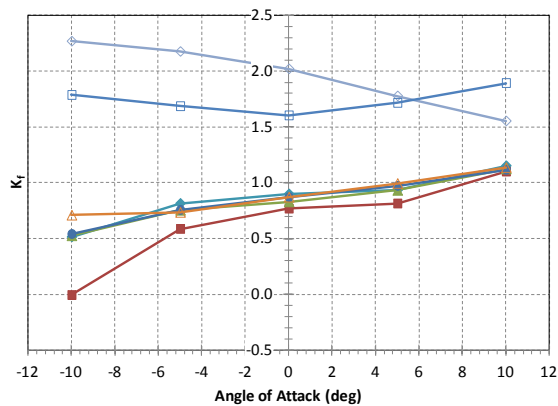
(a)   (b)

Figure 13. (a) Force and (b) moment amplification factor vs. α, Mach 1.5.

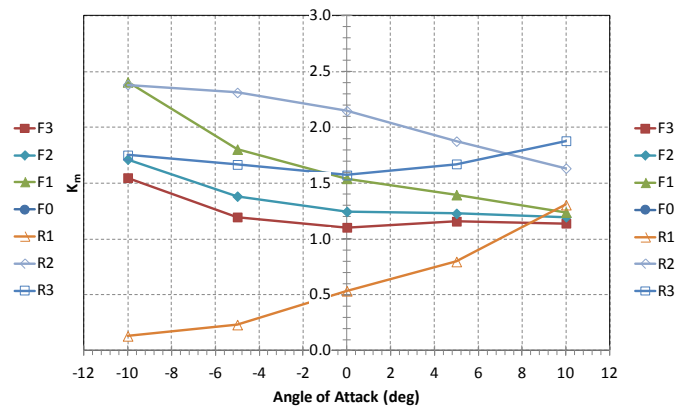(a)   (b)

Figure 14. (a) Force and (b) moment amplification factor vs. α, Mach 2.5.

(a)   (b)

Figure 15. (a) Force and (b) moment amplification factor vs. α, Mach 3.5.
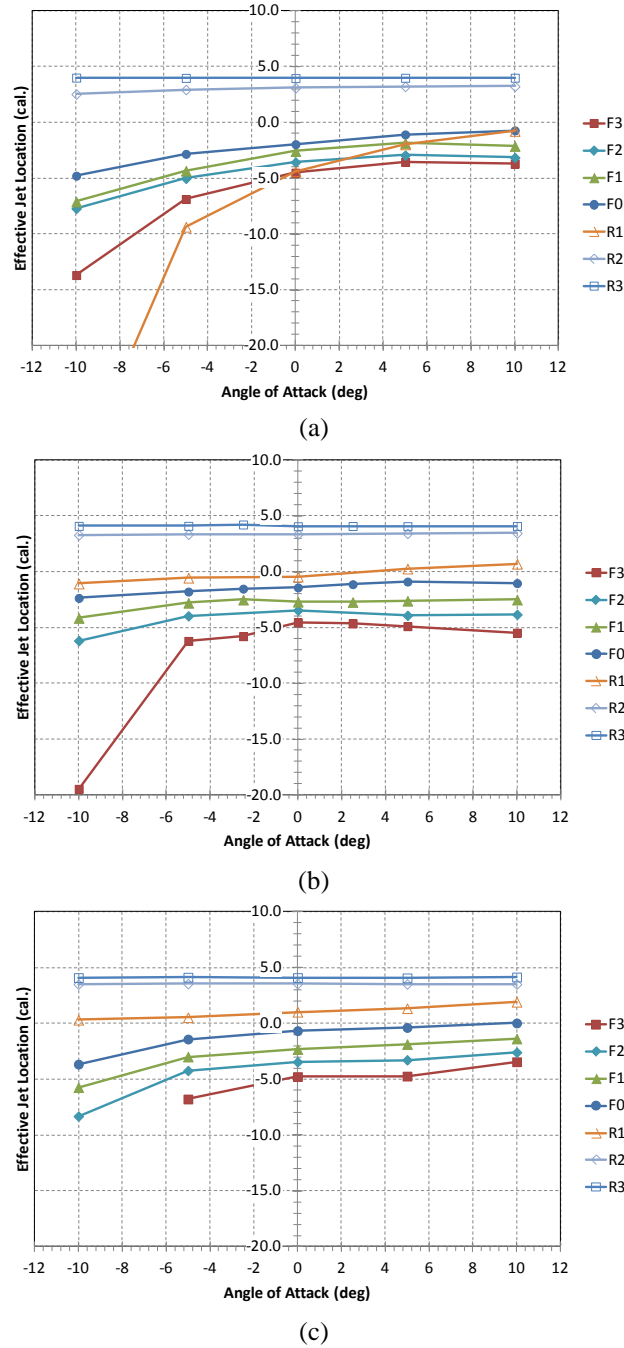
(a)

(b)

(c)

Figure 16. Effective jet location (cal.) vs. α, (a) Mach 1.5, (b) Mach 2.5, and (c) Mach 3.5.

D. Flight Trajectory Simulations

   As mentioned previously, a goal of the present study is to determine if correlations for effective jet force and effective jet location (i.e., jet actuation parameters) can be developed for use in aeroprediction design codes for accurate prediction of the control forces and moments. Currently, unless experimental data already exists for a flight body similar to one of interest, it can be difficult to estimate the effective jet actuation parameters. Most likely flight trajectory simulations would be run with a range of jet actuation parameters to bound the maneuver capability. In the present study, some 6DOF flight trajectory simulations were performed comparing the maneuver response of the

ideal jet, i.e., the unattenuated jet thrust applied at the jet exit, with the *effective* jet $(K_f F_j)$ applied at the calculated effective location, $x_{cp_{eff}}$.

A model of the ANF was generated in the projectile, design, and analysis software PRODAS.[17] The aerodynamic coefficients were predicted within PRODAS and compared well to those in Refs. 7 and 8. The control trajectory module (CONTRAJ) within PRODAS was then used to simulate the firing of reaction jets (squibs) at defined locations and projectile roll orientations. Two sets of simulations were performed—an extended range maneuver and a lateral deflection maneuver. Both sets of simulations assumed an initial launch Mach number of 1.5, a launch quadrant elevation (QE) of 2°, an initial yaw rate of 5 rad/s, and a jet thrust of 215.6 N. A series of two squibs were fired when the projectile was at apogee. The first squib was fired at $t = 1.7$ s and the second was fired 0.1 s later, as the projectile rolled 180° from the orientation of the first squib firing. Although the ANF fins in the CFD simulation are uncanted, a 0.25° cant was assumed in the flight simulations, giving a projectile roll rate of about 10 Hz near apogee. The firing duration of each squib was 0.01 s, giving a jet impulse of 2.16 N-s each.

The roll orientation at which the squib was fired was specified to give an extended range (typically nose up) or deflection to the left (typically nose left). The extended range simulations were performed for each of the seven jet locations investigated in the CFD. The deflection simulations were performed for the jet located at the most forward (F3), projectile c.g. (F0) and most rearward (R3) locations. Tables 4 and 5 provide the amplification factor, the effective jet force, and the jet exit and effective jet location, both referenced from the projectile nose. Table 4 shows the maximum range and maximum total angle of attack, $\alpha_T = \sqrt{\alpha^2 + \beta^2}$, for the extended range maneuver simulations.

The results for the ANF without a jet, or "ballistic," flight trajectory are also given. The ballistic trajectory results in a maximum range of 1580.7 m and a maximum $\alpha_T = 1.4°$ (due to the initial yaw rate). It is noted that the firing of the squib provides a lateral reaction that can be broken into a force acting at the c.g. and a couple located at the c.g., so usually a rotation of the projectile about the c.g. results. This is evident in the values of maximum α_T in Table 4. When the jet is located forward of the c.g., a thrust acting in the direction of the intended maneuver (up) is provided. However, because the nose of the projectile moves in the direction opposite the intended maneuver when the jet is located to the rear of the c.g., a jet thrust in the direction opposite the intended maneuver may provide the intended result. In Table 4, the negative thrust values for the R2 and R3 locations indicates that the squib was directed to fire in the "down" orientation, rather than the "up" orientation used for the other locations. Even though the R1 location is to the rear of the c.g., the distribution of the lateral force and couple located at the c.g. was such that an "up" jet force provided more extended range than a "down" jet force.

Table 4. Results of trajectory simulations for extended range maneuver, F_j = 215.6 N.

Jet Location	K_f	$F_{j_{eff}}$	x_{cp_j}	$x_{cp_{eff}}$	Maximum Range			Maximum α_T		
					Case 1	Case 2	Case 3	Case 1	Case 2	Case 3
		(N)	(mm)	(mm)	(m)	(m)	(m)	(deg)	(deg)	(deg)
No Jet					1580.7	1580.7	1580.7	1.4	1.4	1.4
F3	0.68	146.6	65.0	32.5	1811.8	1762.5	1739.7	13.6	12.3	9.3
F2	0.75	161.7	90.0	60.5	1787.1	1759.4	1735.1	10.2	10.7	7.7
F1	0.68	146.6	127.5	89.7	1743.5	1720.7	1689.4	5.1	7.0	3.5
F0	0.57	122.9	165.0	108.7	1694.5	1684.5	1644.0	1.4	4.4	1.4
R1	0.26	56.1	215.0	39.9	1626.5	1648.9	1592.9	6.8	4.4	1.8
R2	1.06	-228.6	265.0	258.4	1578.7	1571.5	1577.3	13.6	13.4	14.4
R3	1.79	-386.0	290.0	284.2	1598.2	1558.7	1560.7	17.0	28.9	30.3

Three cases were simulated for each jet location. Case 1 was the ideal jet thrust located at the jet exit, Case 2 was the effective jet thrust acting at $x_{cp_{eff}}$, as calculated from CFD results. Case 3 was the effective jet thrust acting at the jet exit, which was considered because one may have an estimate for K_f but not $x_{cp_{eff}}$. The goal was to determine the level of error in the flight trajectory resulting from assuming the jet acts at the jet exit with the un-

modulated thrust force. The percent difference in maximum range between Case 1 and Case 2 for the extended range simulations ranged from 0.5–2.8%. The percent difference in maximum range between Case 3 and Case 2 ranged from 0.1–3.5%, with the minimum and maximum differences occurring at different jet exit locations than those between Cases 1 and 2. These percent differences are not very large, but the maximum difference in range was 49.3 m, which is larger than the desired accuracy for precision guided munitions. Maximum α_T values are attained when the jet is located farthest from the c.g. The maximum α_T is attained when the jet is located at the R3 location because the jet is amplified ($K_f > 1.0$) there.

Table 5 shows similar results for the deflection maneuver simulations with the jet located at the F3, F0, and R3 locations. The resulting total angle of attack values are the same as for the extended range maneuver. There were only small effects on maximum range (not shown) due to the lateral deflection maneuver. The percent difference in lateral deflection between Case 1 and Case 2 ranged from 8–36% (0.3–1.9 m). The percent difference in lateral deflection between Case 3 and Case 2 ranged from 16–63% (0.3–1.6 m), with the minimum and maximum differences again occurring at different jet exit locations than those between Cases 1 and 2.

The error in deflection due to incorrect jet thrust force and location are fairly large. Also, the error can build as more multiple thrusters are used over the course of the complete trajectory. These results indicate that it is obviously better to used the effective jet thrust and effect jet location if available. If K_f is available but $x_{cp_{eff}}$ is not, at most locations it is better to then use the effective jet thrust acting at the jet exit location. Time did not permit a similar evaluation at higher Mach numbers or with longer jet duration (larger impulse) squibs.

Table 5. Results of trajectory simulations for left deflection maneuver, $F_j = 215.6$ N.

Jet Location	K_f	$F_{j_{eff}}$	x_{cp_j}	$x_{cp_{eff}}$	Maximum Deflection			Maximum α_T		
					Case 1	Case 2	Case 3	Case 1	Case 2	Case 3
		(N)	(mm)	(mm)	(m)	(m)	(m)	(deg)	(deg)	(deg)
No Jet					0.01	0.01	0.01	1.4	1.4	1.4
F3	0.68	146.6	65.0	32.5	9.38	7.51	6.49	13.6	12.3	9.3
F0	0.57	122.9	165.0	108.7	4.58	4.24	2.61	1.4	4.4	1.4
R3	1.79	-386.0	290.0	284.2	1.47	1.09	1.38	17.0	28.9	30.3

Figure 17a shows the flight trajectory for the extended range simulation with the jet at the F3 location. The three jet cases and the ballistic case are shown. The ideal jet (Case 1) over predicts the maximum range that would be attained using the effective jet (Case 2). At this location, there is a small difference between Case 3 and Case 2. Figure 17b shows the total angle of attack for these cases. Note that the second squib fires while the projectile body is at an angle of attack of about 6°–8°. The effective jet thrust and $x_{cp_{eff}}$ values could have been adjusted for the second squib to account for this angle. Alternatively, a better solution is for the second squib to be timed to occur when α_T is near zero.

Figure 18 shows the lateral deflection predicted for the deflection maneuver with the jet located at the F3 (Fig. 18a) and the R3 (Fig. 18b) jet exit locations. When the jet is located at the F3 location, the Case 1 simulation again over predicts the deflection and the Case 3 simulation under predicts the deflection, but by less of a margin. When the jet is located at the R3 location, both the Case 1 and Case 3 simulations over predict the deflection, but the maximum deflection is about an order of magnitude less than when the jet is located at the F3 location. Figure 18c shows the total angle of attack for the cases when the jet is located at the R3 location. The maximum angles are about two times those for when the jet is located at the F3 location (Fig. 17b).

The results shown in Tables 4 and 5 demonstrate that the largest control maneuver is attained when the jet is located at the nose of the projectile. Fresconi and Plostins[18] showed that the aft end of a spin-stabilized projectile is the optimum location for control actuators. A similar analysis shows that the optimum location for a control actuator on a fin-stabilized projectile is the front section of the projectile. In practical situations the designer may be limited to where the jet can be located due to other considerations for payload, GN&C components etc. However, locating the jet near the projectile base can have the advantage of minimizing the error in the effective jet location, but the maneuver control authority will not be the optimum.
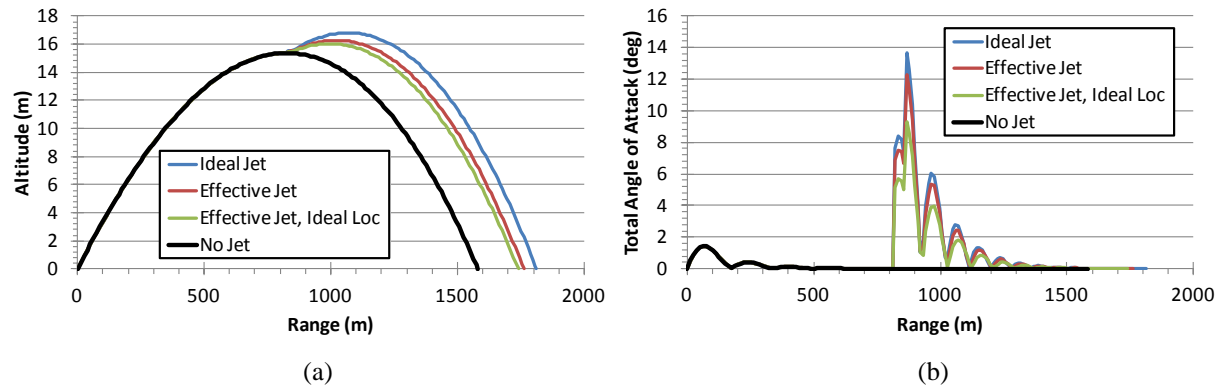
(a)   (b)

Figure 17. Extended range trajectory simulation at Mach 1.5 for jet at F3 location: (a) altitude vs. range, and (b) total angle of attack vs. range.

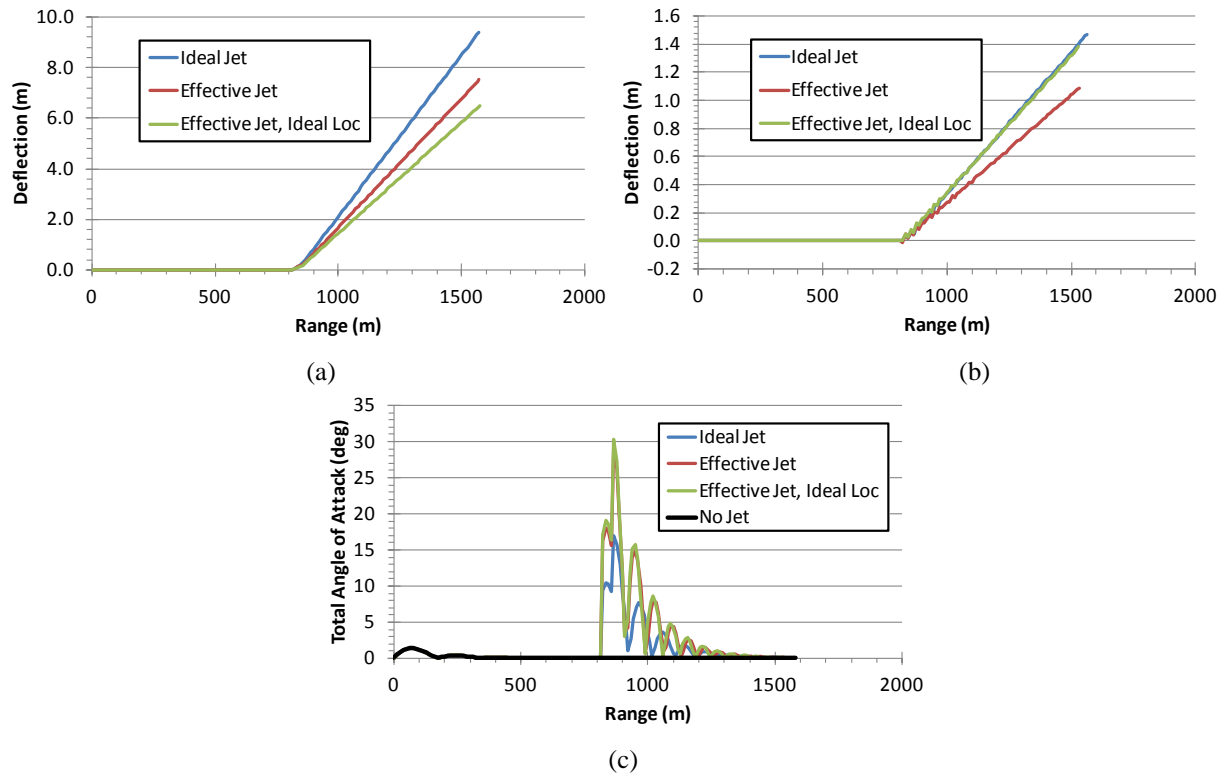(a)   (b)

(c)

Figure 18. Left deflection trajectory simulation at Mach 1.5: deflection vs. range for jet at (a) F3 location and (b) R3 location, and (c) total angle of attack vs. range for jet at R3 location.

IV. Summary and Future Work

The study reported in Ref. 5 was extended to include data at $\alpha = 0°$ and Mach 3.5 and data at $-10° \leq \alpha \leq 10°$ at Mach 1.5, 2.5, and 3.5. At $\alpha = 0°$, there is less variation of K_f at the higher Mach numbers but the general trends are similar for each Mach number investigated. Flowfield visualizations indicated the size of the jet plume and the size of the resulting low-pressure region behind the jet was reduced as Mach number increased. This is primarily due to the increased dynamic pressure of the freestream flow at the higher Mach numbers.

Flowfield visualizations of the cases with $-10° \leq \alpha \leq 10°$ showed that the counter rotating vortex pair (CVP) generated by the jet plume was pushed very close to the tail fins at the high negative angle of attack when the jet exit was located forward of the tail fins. At high positive angles of attack, the CVP moved away from the body relatively quickly. These qualitative observations are consistent with the data for K_f showing that there was more variation as the angle of attack became more negative. The effective jet location, $x_{cp_{eff}}$, varied little for $\alpha > -5°$ at Mach 2.5 and 3.5.

Flight simulations using reaction jet "squibs" were performed to evaluate the sensitivity of the control maneuver to the differences in jet thrust and jet actuation location. The results indicated that more accurate results were obtained if the effective jet thrust and effective jet location were used rather than the values for the *ideal* jet. Reasonable results could be obtained if the effective jet thrust was used at the ideal jet location (jet exit) for the case where an estimate for $x_{cp_{eff}}$ is unknown.

Additional work is planned to further analyze the data generated thus far to determine if correlations exist to enable predicting the K_f and $x_{cp_{eff}}$ values. Work is also planned to investigate transient effects of a pulsed jet, with and without projectile roll, to determine if the JI predicted from steady state simulations are the same in unsteady flowfields.

Acknowledgments

References

[1]Margason, R. J., "Fifty Years of Jet in Cross Flow Research," AGARD, *72nd Fluid Dynamics Panel Meeting*, Paper 1, 1993

[2]Spaid, F. W., and Cassel, L., A., "Aerodynamics Interference Induced by Reaction Controls," AGARDograph No. 173, Dec. 1973

[3]Champigny, P., and Lacau, R. G., "Lateral Jet Control for Tactical Missiles," *Special Course on Missile Aerodynamics*, AGARD-R-804, Paper 3, 1994.

[4]Graham, M. J., and Weinacht, P., "Numerical Investigation of Supersonic Jet Interaction for Axisymmetric Bodies," *Journal of Spacecraft and Rockets*, Vol. 37, No. 7, 2000, pp. 675–683.

[5]DeSpirito, J., "Factors Affecting Reaction Jet Interaction Effects on Projectiles," AIAA-2011-3031, June 2011.

[6]DeSpirito, J., "Numerical Investigation of Lateral Jet Interaction on a Fin-Stabilized Projectile," *Proceedings of the 26th International Symposium on Ballistics*, Miami, FL, September 2011.

[7]Dupuis, A. D., "Aeroballistic Range and Wind Tunnel Tests of the Basic Finner Reference Projectile from Subsonic to High Supersonic Velocities," TM-2002-137, Defence R&D Canada Valcartier, Canada, Oct. 2002.

[8]Dupuis, A. D., and Hathaway, W., "Aeroballistic Range Tests of the Basic Finner Reference Projectile at Supersonic Velocities," DREV-TM-9703, Defence Research Establishment, Valcartier, Canada, Aug 1997.

[9]Metacomp Technologies, Inc., "MIME User Manual," Agoura Hills, CA, 2008.

[10]Metacomp Technologies, Inc., "CFD ++ User Manual," Agoura Hills, CA, 2010.

[11]Menter, F. R., "Two-Equation Eddy-Viscosity Turbulence Models For Engineering Applications," *AIAA Journal*, Vol 32, No. 8, 1994, pp. 1598–1605.

[12]Spalart, P R, Allmaras, S R, "A One-Equation Turbulence Model for Aerodynamic Flows," Recherche Aerospatiale, No 1, pp 5–21, 1994.

[13]Chien, K-Y, "Predictions of Channel and Boundary Layer Flows with a Low-Reynolds-Number Turbulence Model," AIAA Journal, Vol 20, No 1, 1982.

[14]Goldberg U, Batten, P, Palaniswamy, S, Chakravarthy, S, Peroomian, O, "Hypersonic Flow Predictions Using Linear and Nonlinear Turbulence Closures," AIAA Journal of Aircraft Vol 37, No 4, July/August 2000.

[15]Goldberg U, Peroomian, O, Chakravarthy, S, "Application Of The k-ε-R Turbulence Model To Wall-Bounded Compressive Flows," AIAA 98-0323, January 1998.

[16]Batten P, Craft T J, Leschziner M A, and Loyau H, "Reynolds-stress-transport modeling for compressible aerodynamics applications, AIAA Journal, Vol 37, No 7, July 1999.

[17]Arrow Tech Associates, 1233 Shelburne Rd, Suite D8, South Burlington, VT 05403

[18]Fresconi, F., and Plostins, P., "Control Mechanism Strategies for Spin-Stabilized Projectiles," *J. Aerospace Engineering*, Vol. 224, No. G9, pp. 979–991, 2010.